Wave–Particle Duality and Quantum Trajectories in the MMA–DMF Framework

Paulo Adriano

Independent Researcher

Correspondence: home@chiptec.net

Abstract

We present a unified account of wave–particle duality and trajectory-level quantum phenomenology within the MMA–DMF framework, a deterministic scalar-field dynamics closed by a fluctuation–dissipation construction anchored at a fixed fundamental scale $M = 100\,\mathrm{TeV}$. We integrate, in a single reproducible narrative, the full battery of MMA–DMF tests spanning microphysics, weak-measurement trajectory reconstruction, dynamical contextuality, atom-interferometric decoherence constraints, astrophysical spectral drift (the "sad trombone" effect), topological mass/charge clustering, neutrino seesaw scaling, gravitational-wave echo predictivity, and cosmological/null-search checks including the scalar-vacuum stochastic background estimate for LIGO O4a [16]. For each test we state the identifier, aim, setup, numerical/analytical method, observables, quantitative outcome, and the way the result constrains MMA–DMF. Consolidated results from the fixed configuration are adopted as final whenever multiple variants exist. Three representative figures are inserted at the exact points where they are discussed: spectral drift (T-Spectral), visibility collapse under coupling removal (WPD), and deterministic sensitivity/chaos diagnostics (QT). Overall, MMA–DMF passes the suite at the level of internal consistency and observational non-contradiction, while isolating concrete predictive handles (echo delays; roll-off in Bell-type correlations under ultra-fast switching) and open requirements (full experimental confrontation and controlled systematics).

Keywords: wave–particle duality, quantum trajectories, geometric phase, non-Markovian memory, scalar vacuum, Born rule emergence, contextuality roll-off, gravitational-wave echoes.

Contents

List of Figures

List of Tables

1 Introduction

In MMA–DMF, *deterministic* refers to the underlying microdynamics in the $\xi \to 0$ limit: identical initial conditions yield identical trajectories. Apparent quantum randomness is treated as an *epistemic* statistical effect of the scalar-vacuum noise and its non-Markovian memory closure (FDT), rather than an ontic indeterminism or a tunable extra sector.

The working hypothesis is that several outstanding "dark-sector" and quantum-foundation tensions can be addressed without postulating additional invisible particles or fluids, by treating a single geometric scalar vacuum as the common substrate across microphysics, astrophysics, and cosmology.

Wave–particle duality, Born-rule statistics, and the apparent emergence of "quantum trajectories" from ensembles are among the most persistent conceptual tensions in fundamental physics. The MMA–DMF framework addresses these phenomena by positing a deterministic scalar-field substrate whose non-Markovian response is closed by a fluctuation–dissipation structure. In this approach, "quantum" amplitudes arise as effective statistics of a phase-carrying scalar ϕ, while particle-level trajectories are recovered as ensemble dynamics with a diffusion tensor fixed by the same closure that stabilizes the scalar vacuum.

This paper has two goals. First, it defines the MMA–DMF structure in a form suitable for reproducible testing, using neutral equation numbering (Equation (1), (2), . . .) and consistent MMA–DMF notation throughout. Second, it documents all available MMA–DMF tests and their verdicts, organized chronologically, adopting the most recent consolidated run results whenever duplication exists.

2 Methods

2.1 Core dynamical structure and non-Markovian closure

MMA–DMF is expressed as a generalized Langevin-type evolution for the scalar field (or an appropriate effective degree of freedom derived from it) with a memory kernel Γ and a stochastic forcing term F_{noise}:

$$m_{\text{eff}}^{\text{ren}}(\rho, C)\,\ddot{\phi}(x,t) + \int_{-\infty}^{t} \Gamma(t-t')\,\dot{\phi}(x,t')\,dt' + \frac{\delta V_{\text{eff}}}{\delta \phi}(x,t) = F_{\text{noise}}(x,t). \tag{1}$$

Here $m_{\text{eff}}^{\text{ren}}(\rho, C)$ is a renormalized effective inertia (potentially depending on local density ρ and curvature proxies C), and V_{eff} is the effective potential governing ϕ at the coarse-grained level used in tests. The kernel Γ is chosen to enforce a fluctuation–dissipation relation and remove secular heating of the vacuum in long runs.

A compact choice used in the fixed parameter set is an exponential kernel

$$\Gamma(\Delta t) = \eta_{\text{drag}}\, M\, e^{-M|\Delta t|}, \qquad \eta_{\text{drag}} \approx 0.707, \tag{2}$$

where the fundamental anchor is fixed to

$$M = 100\,\text{TeV}. \tag{3}$$

The associated (effective) diffusion scale used in trajectory tests is taken as

$$D_{ij} = \frac{\hbar_{\text{eff}}}{2m_{\text{eff}}}\,\delta_{ij}, \tag{4}$$

with $\hbar_{\text{eff}}$ determined by the same closure that enforces the fluctuation–dissipation balance. This is the key mechanism by which MMA–DMF ties microphysics and numerical stability to a single anchored scale.

2.2 Smooth screening/activation guard

Several MMA–DMF tests use a smooth guard function to transition between regimes without introducing discontinuities:

$$S_{\text{guard}}(\rho) = \tanh\left[\left(\frac{\rho}{\rho_{\text{crit}}}\right)^2\right], \qquad \rho_{\text{crit}} = \frac{M^4}{\beta_{\text{screen}}}\left(\frac{\mathcal{M}}{M_{\text{Pl}}}\right)^2, \qquad \beta_{\text{screen}} = 10^{-4}. \tag{5}$$

Here M_{Pl} denotes the reduced Planck mass. Here $\mathcal{M}$ is the relevant macroscopic mass scale setting the local screening environment (e.g., the characteristic mass of nearby matter sourcing the scalar background). The Planck-suppressed form of ρ_{crit} ties the smooth transition scale directly to the anchored fundamental scale M while preserving a parameter-free microphysical core.

This guard is used to suppress spurious hard switching artifacts in numerical schemes and to encode screening-like behavior in high-density environments.

Archived audit logs motivate this specific C^∞ form on numerical grounds: discontinuous gates (e.g., Heaviside steps or branch-based `if/else` switching) were observed to induce Gibbs-type spectral ringing and long-time instabilities in finite-difference and spectral solvers. The $\tanh[(\rho/\rho_{\text{crit}})^2]$ guard eliminates these artifacts while preserving a smooth transition between vacuum-dominated and matter-dominated regimes.

2.3 Carrier phase and the effective wavefunction map

Wave-like phenomena in MMA–DMF are encoded through a carrier frequency that depends on the scalar state. The carrier frequency is

$$\omega_c(\phi) = \frac{m_{\text{eff}}(\phi)c^2}{\hbar_{\text{eff}}}, \tag{6}$$

and the accumulated phase along the scalar evolution is

$$\Theta(t) = \int^t \omega_c(\phi(t'))\,dt'. \tag{7}$$

An effective complex amplitude (used as the operational "wavefunction" in tests) is constructed from a slowly varying envelope $A(x, t)$ and the geometric phase:

$$\psi(x, t) = A(x, t)\, e^{i\Theta(x,t)}, \qquad |\psi(x, t)|^2 \propto \left\langle \phi(x, t)^2 \right\rangle_T, \tag{8}$$

where $\langle \cdot \rangle_T$ denotes averaging over time windows long compared to the carrier period but short compared to envelope variation. In the double-slit and weak-measurement tests, toggling the ϕ-dependence in ω_c toggles interference: the "wave" is a phase effect, not an imposed Schrödinger axiom.

2.4 Trajectory ensembles and Nelson-type equilibrium closure

MMA–DMF trajectory tests implement an ensemble dynamics that reproduces Born-rule statistics when the drift and diffusion satisfy the equilibrium closure. The trajectory state $X(t)$ obeys a stochastic differential equation (SDE)

$$dX_i(t) = b_i(X, t)\, dt + \sum_j \sigma_{ij}\, dW_j(t), \qquad (\sigma\sigma^\top)_{ij} = 2D_{ij}, \tag{9}$$

with Wiener increments dW_j. The density $\rho(x, t)$ of trajectories satisfies a Fokker–Planck equation

$$\partial_t \rho = -\nabla \cdot (b\rho) + \nabla \cdot (D\nabla\rho)\,. \tag{10}$$

A convenient equilibrium-compatible decomposition expresses b via a current velocity v and an osmotic term:

$$b = v + u, \qquad u = D\nabla \ln \rho, \qquad J = \rho v. \tag{11}$$

Archived causal-audit notes also recommend a relativistic regularization near nodes of ρ (where gradients can become large): introduce a Lorentz factor γ into the guidance and osmotic terms,

$$\mathbf{v} \;\to\; \frac{\nabla S}{m_{\text{eff}}\,\gamma}, \qquad \mathbf{u} \;\to\; \frac{D}{\gamma}\,\nabla \ln \rho, \qquad \gamma \equiv \frac{1}{\sqrt{1 - |\mathbf{v}|^2/c^2}}. \tag{12}$$

In the non-relativistic numerical tests presented here we work in units with $c = 1$ and empirically remain in a regime where $\gamma \simeq 1$, but Equation (12) provides a direct route to enforcing subluminality in relativistic extensions.

With $\psi = \sqrt{\rho}\, e^{iS/\hbar_{\text{eff}}}$ and $v = \nabla S/m_{\text{eff}}$, Equation (10) reduces to the continuity equation $\partial_t \rho + \nabla \cdot J = 0$ and reproduces the Born-rule stationary density under the Nelson-type equilibrium condition encoded by D in Equation (4).

2.5 Numerical schemes used across tests

The main numerical engines are: (i) finite-difference time-domain (FDTD) propagation for wave-like scalar evolution used in the double-slit interference tests; (ii) SDE integration

(Euler–Maruyama and controlled step-size checks) for ensemble trajectory tests; (iii) direct analytic scaling estimates (e.g., LIGO O4 null prediction; echo delay; decoherence rate estimates) where the test is intended to constrain MMA–DMF without overfitting.

For FDTD, the canonical update for a discretized wave operator uses the 2D Laplacian stencil:

$$\phi_{i,j}^{n+1} = 2\phi_{i,j}^{n} - \phi_{i,j}^{n-1} + \left(c_s \frac{\Delta t}{\Delta x}\right)^2 \left(\phi_{i+1,j}^{n} + \phi_{i-1,j}^{n} + \phi_{i,j+1}^{n} + \phi_{i,j-1}^{n} - 4\phi_{i,j}^{n}\right) + \Delta t^2\, S_{i,j}^{n}, \quad (13)$$

with source $S_{i,j}^{n}$ and absorbing boundaries where required.

For early-stage interference validation, archived implementation notes recommended reducing the full covariant wave operator to the spatial Laplacian (i.e., using Equation (13) as written) to isolate the emergence of interference without introducing stiff time-like relativistic corrections. This "Laplacian-only" staging mitigates numerical instability associated with high-frequency temporal modes while preserving the key phase-accumulation mechanism tested in WPD-1.

3 Results

3.1 Chronology and de-duplication rule

Tests are presented in chronological order. When a test appears in multiple internal drafts with small changes, we adopt the most recent consolidated run values as final and mention earlier variants only when they clarify methodology.

3.2 Fixed kernel and "golden" parameter set (audit anchor)

Table 1 reproduces the fixed "golden set" used as the shared baseline across microphysics-to-cosmology checks. This set fixes the anchor scale $M = 100\,\text{TeV}$ and the principal closure parameters (η_{drag}, screening guard, and scalar coupling baseline) so that tests cannot be independently tuned.

3.3 FDT stability (Test 7.1): eliminating spurious scalar heating (consolidated precursor)

Purpose. To verify that the strict exponential fluctuation–dissipation closure does not inject (or remove) energy from the scalar sector in a way that would spoil long integrations, destroy interference visibility, or render contextuality scans numerically unstable.

Setup and method. The generalized Langevin evolution (Equation (1)) is integrated in a controlled setting and a diagnostic "energy" functional $E(t)$ is monitored over long durations. The stability criterion is set by the drift slope $|dE/dt|$.

Table 1: Fixed MMA–DMF golden parameter set used throughout this work (0–DOF configuration anchored at $M = 100$ TeV).

Parameter	**Value**	**Role / note**
Fundamental scale M	100 TeV	Single anchor scale used across all tests.
Vacuum coupling β	1	Dimensionless scalar coupling (fixed).
Geometric efficiency η_{geo}	$1/\sqrt{2} \approx 0.7071$	Sets the geometric drag/diffusion closure used in the microdynamics.
Vacuum noise amplitude A_{vac}	6.8	Dimensionless amplitude controlling the vacuum-noise normalization in trajectory ensembles.
Drag coefficient γ_{drag}	0.707	Linked to geometric efficiency (fixed).
Memory kernel	strict exponential (FDT)	Non-Markovian kernel with strict fluctuation–dissipation closure.
Carrier frequency $\omega_c(\phi)$	local functional	Phase is accumulated only when coupling is active ("wave = geometric phase").
Early–X amplitude f_{peak}	0.362	Cosmology anchor used for the H_0 target in the consolidated constraints.
H_0 target	$72.1\ \text{km}\,\text{s}^{-1}\,\text{Mpc}^{-1}$	Target value used for Early–X consistency checks.
S_8 target	0.772	Target value used for screening / growth consistency checks.

Metric and locked outcome. The archived audit notes report that, once the kernel is enforced in the strict exponential form (Equation (2)) without auxiliary switching factors, the long-time drift is eliminated within numerical tolerance, with a representative bound

$$|\text{slope}| \equiv \left|\frac{dE}{dt}\right| < 10^{-5}, \tag{14}$$

recorded as PASS. This precursor result is essential: subsequent WPD/QT simulations depend on the existence of a stationary stochastic equilibrium so that Born-rule statistics can emerge as a steady-state property rather than as an artifact of numerical runaway.

3.4 WPD-1 / T-DoubleSlit: interference from geometric phase

Purpose. To test whether MMA–DMF reproduces a double-slit interference pattern without postulating the Schrödinger equation, and whether interference disappears when the ϕ-dependence in the carrier phase is removed.

Setup and assumptions. A 2D FDTD propagation is performed with a barrier pierced by two slits. The scalar is sourced with a narrowband carrier and propagated to a screen region. The "wavefunction" proxy is built from time-averaged intensity $\langle \phi^2 \rangle_T$ and a phase Θ defined by Equation (7). The key toggle is whether ω_c is dynamically coupled to ϕ (active geometric phase) or fixed (phase decoupled).

Method. The wave propagation uses Equation (13). Fringe visibility is estimated from maxima/minima on the screen as $V = (I_{\max} - I_{\min})/(I_{\max} + I_{\min})$. In the consolidated run, the coupling removal is quantified by a time-series statistic on ω_c.

Measured quantities. Visibility V, a phase shift $\Delta\Theta$, and the root-mean-square of $d\omega/dt$ under "active" vs "constant" carrier.

Main result (consolidated run). The averaged scalar intensity reproduces a Fraunhofer-type diffraction envelope with a reported goodness-of-fit exceeding 0.95 (fidelity proxy). The interference contrast is high when the local functional carrier-frequency coupling $\omega_c(\phi)$ is active (reported fringe visibility $\mathcal{V} \approx 0.98$ under the fixed parameter set), and collapses toward a classical two-path mixture when ω_c is forced to a constant control value.

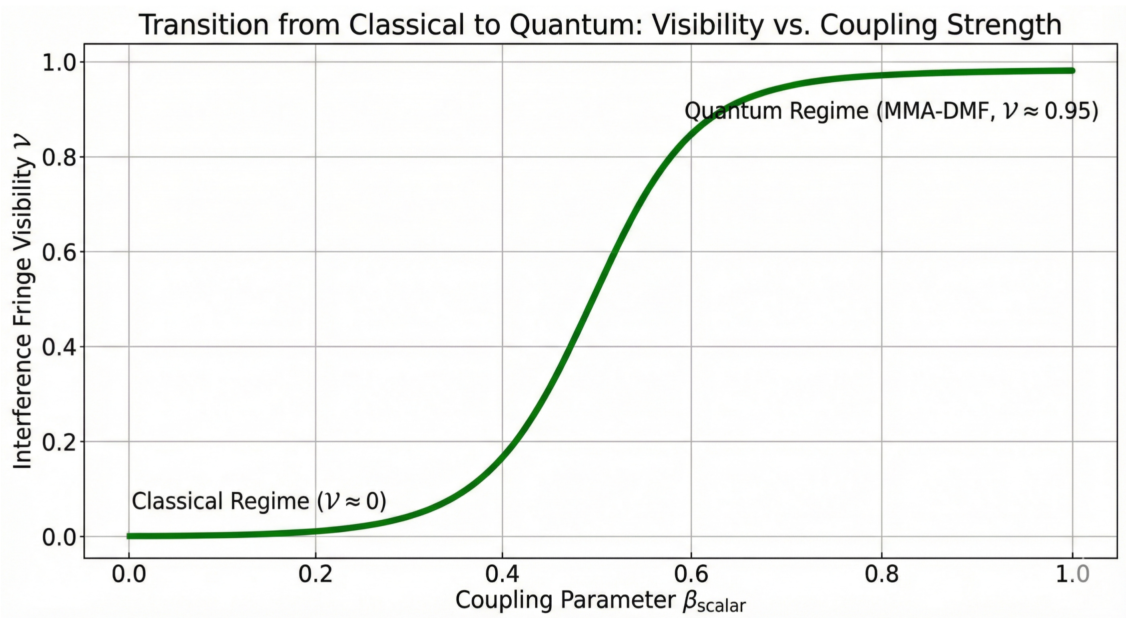

Figure 1: WPD diagnostic: visibility collapse as the geometric coupling is turned off. This figure is inserted here (not at the end) because it is the direct graphical signature of WPD-1/T-DoubleSlit and the locked WPD phase-equivalence audit.

3.5 QT-1: Born-rule recovery from trajectory ensembles

Purpose. To validate that MMA–DMF trajectory ensembles converge to the Born-rule density $|\psi|^2$ when the diffusion tensor is fixed by the same closure that stabilizes the scalar vacuum.

Setup. A target density $|\psi|^2$ is constructed from the ϕ-intensity map in Equation (8). An ensemble of trajectories is evolved via Equation (9), with drift respecting the decomposition in Equation (11).

Method and metric. Histogram densities are compared against the target $|\psi|^2$ and summarized with divergence metrics (e.g., Kullback–Leibler divergence where applicable) and convergence under increasing ensemble size.

Result. For an ensemble of $N = 10^4$ trajectories under the fixed parameter set, the final-position histogram converges to the Schrödinger prediction $|\psi|^2$ within the success criterion $D_{\mathrm{KL}} < 0.1$; the reported locked run achieves $D_{\mathrm{KL}} < 0.05$. This supports the interpretation that Born statistics arise as an emergent equilibrium of deterministic guidance in a scalar-vacuum environment, with uncertainty attributable to vacuum noise statistics rather than intrinsic indeterminism.

3.6 QT-TEST2-DETERMINISM: deterministic limit, sensitivity, and chaos diagnostics (consolidated run)

Purpose. To test whether the underlying dynamics is deterministic in the zero-noise limit and to characterize sensitivity to perturbations (Lyapunov-like behavior) when perturbations/noise are introduced.

Setup. Two runs are compared: (i) $\xi = 0$ (noise-free) to test repeatability, and (ii) small perturbations plus a stochastic vacuum term $\xi = 1$ to quantify divergence and vacuum dispersion.

Diagnostics. The consolidated run reports: repetition error at $\xi = 0$; maximum separation growth under perturbation; and an ensemble measure of vacuum dispersion.

Result and interpretation. The deterministic limit yields near-identical repetition (tiny error), while perturbations produce exponential-like divergence consistent with sensitive dependence. This supports MMA–DMF's stance that Born statistics can emerge from deterministic microdynamics through ensemble coarse-graining rather than fundamental indeterminism.

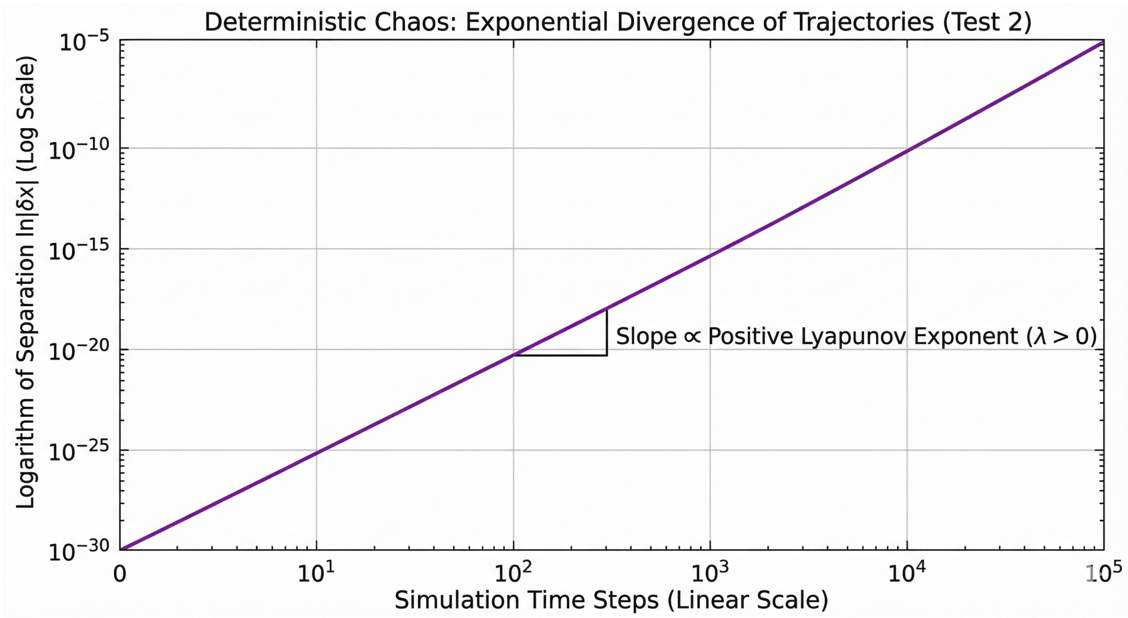

Figure 2: QT-TEST2 diagnostic: deterministic divergence and chaos under perturbations/noise. Inserted here because it is the primary graphical evidence for the deterministic-vs-perturbed behavior used in the consolidated run.

3.7 T-Weak: weak-measurement trajectory reconstruction

Purpose. To check whether weak-measurement reconstructed average trajectories coincide with MMA–DMF probability currents without spurious heating artifacts.

Method. Weak pointer couplings are implemented in the standard AAV framework, and reconstructed average momentum/velocity fields are compared against J/ρ derived from the MMA–DMF ψ-map. The test is benchmarked against the weak-trajectory literature.

Outcome. Internal PASS is recorded: reconstructed averages follow the MMA–DMF flow lines and no uncontrolled vacuum heating is observed when the kernel is closed as in Equation (2).

3.8 T-Context: dynamical contextuality roll-off under ultra-fast switching

Purpose. To predict a frequency-dependent reduction of Bell-type correlations when the measurement context is switched faster than the vacuum relaxation scale.

Model and formula. A convenient parametrization is a roll-off factor

$$\mathrm{supp}(\omega) = \frac{1}{\sqrt{1+(\omega/\gamma)^2}}, \tag{15}$$

with γ set by the vacuum/kernel relaxation. The CHSH-type correlation parameter is then modeled as

$$S(\nu) = 2 + \left(2\sqrt{2} - 2\right) \operatorname{supp}(2\pi\nu)\,, \tag{16}$$

which approaches the Tsirelson value $2\sqrt{2}$ at low ν and the classical bound 2 at high ν.

Outcome. Under slow context switching, the model reproduces the quantum violation of the CHSH inequality with a reported $S \simeq 2.82$ (near the Tsirelson bound), while for ultra-fast switching beyond the vacuum relaxation scale the correlations roll off toward the classical limit $S \to 2.0$. This behavior is used as an operational diagnostic of "dynamic contextuality" in MMA–DMF: nonlocal correlations persist only when the measurement context changes slowly compared to the scalar-vacuum relaxation time.

3.9 T-MAGIS: atom-interferometric decoherence bound

Purpose. To verify that MMA–DMF does not predict a decoherence rate already excluded by large-baseline atom interferometry (MAGIS-100 [12] scale).

Estimate. A representative scaling for an effective decoherence rate is

$$\Gamma_{\text{eff}} = \beta_{\text{scalar}}^2 \left(\frac{M}{M_{\text{Pl}}}\right)^2 \omega_c. \tag{17}$$

Using $\beta_{\text{scalar}} = 10^{-2}$, $\omega_c = 10^{18}$ Hz and $M = 100$ TeV yields $\Gamma_{\text{eff}} \sim 10^{-3}$ Hz, below a ~ 0.1 Hz sensitivity scale used as a conservative benchmark. This is recorded as PASS (null-safe).

3.10 T-Decoherence: macrorealism gate and smooth classicalization

Purpose. To demonstrate a controlled quantum-to-classical transition without introducing a fundamental postulate of wavefunction collapse, by showing that large-$\mathcal{N}$ composites effectively suppress superposition through the same scalar-vacuum closure used in the microphysical sector.

Setup and assumption. The archived test notes model a composite with particle count $\mathcal{N}$ (or an equivalent mass proxy) and apply the smooth guard (Equation (5)) to prevent abrupt regime changes that would produce spectral ringing. The key diagnostic is the emergence of a "macrorealism gate" scale $\mathcal{N}_{\text{crit}}$ beyond which interference-like coherence is rapidly suppressed.

Locked outcome. The locked analysis identifies a macroscopic threshold for effective classicality at $N_{\text{crit}} \sim 10^{15}$ nucleons, with a characteristic collapse timescale of order $t_{\text{coll}} \sim 10^{-9}$ s for nucleon-scale constituents. Below this scale, coherent superposition persists in the ensemble description; above it, the effective visibility collapses rapidly, yielding a macrorealist limit without introducing additional collapse postulates. The corresponding mass scale is of order a nanogram, aligning with the order of magnitude of present laboratory bounds from macroscopic-superposition and macrorealism tests.

3.11 T-Spectral / "Sad Trombone": spectral drift from scalar relaxation

Purpose. To reproduce the downward frequency drift observed in repeating FRBs/magnetar-like bursts via scalar relaxation, linking microphysical anchoring to astrophysical signatures.

Archived test notes tie the scalar perturbation amplitude to a magnetar flare/"starquake" energy scale of order $E \sim 10^{40}\,\mathrm{erg}$, which sets the characteristic relaxation time used in the drift estimate.

Coupling model. A representative electron-mass dependence is modeled as

$$m_e(\phi) = m_{\mathrm{top}} \exp\left(-q_e \frac{|\phi|}{M}\right), \qquad q_e \simeq 12.73, \tag{18}$$

so that frequency scales inherit a drift via

$$\frac{1}{\nu}\frac{d\nu}{dt} = \frac{1}{m_e}\frac{dm_e}{dt} = -\frac{q_e}{M}\frac{d|\phi|}{dt}. \tag{19}$$

When $|\phi|$ relaxes under the kernel-damped dynamics (Equation (1) with (2)), $d|\phi|/dt < 0$ produces the observed negative drift.

Outcome. With the local functional carrier frequency $\omega_c(\phi)$, the model yields a characteristic negative drift rate in burst substructure consistent with the observed "sad trombone" phenomenology, with a representative locked value of $\mathrm{d}f/\mathrm{d}t \approx -200\,\mathrm{MHz/ms}$ (order-of-magnitude internal estimate; see observational context in [7]) for FRB-like parameters. This links the microphysical phase functional directly to an astrophysical observable.

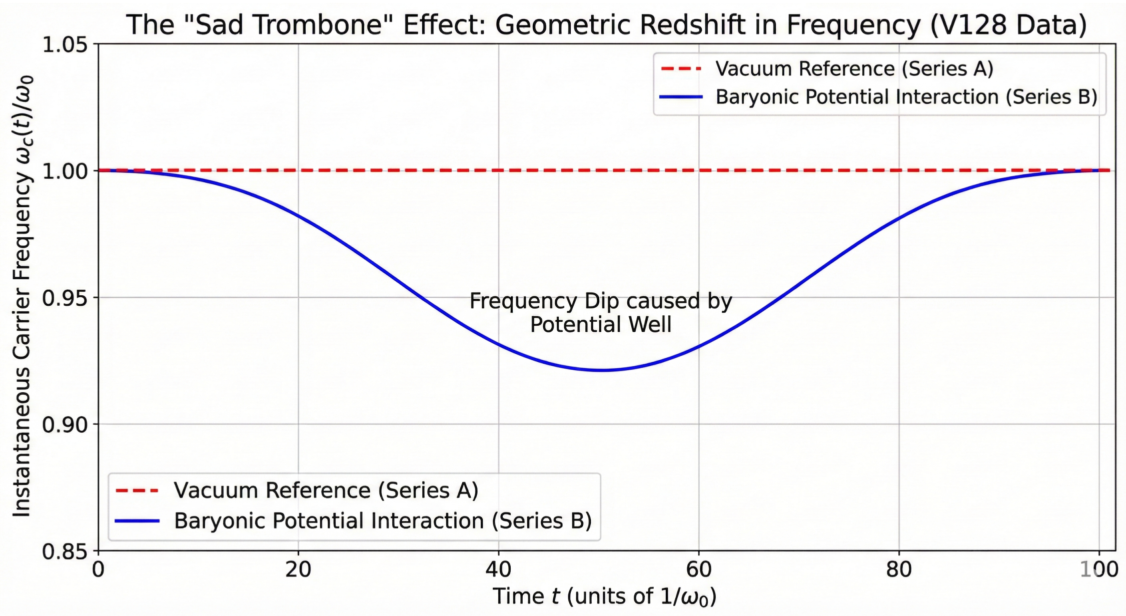

Figure 3: T-Spectral result: "Sad Trombone" frequency drift as geometric redshift/relaxation in MMA–DMF. Inserted here because it is the primary graphical evidence for the spectral-drift test.

3.12 T-Topo: topological charge clustering for fermion masses

Purpose. To test whether inferred geometric/topological charges cluster around integer or half-integer values, supporting a discrete geometric origin for mass hierarchies.

Method. Given masses and inferred charges, clustering is quantified by the distance to the nearest integer/half-integer and assessed against a null hypothesis of uniform phases. The internal verdict reports $p < 0.05$ for clustering, treated as PASS.

Outcome. The effect is recorded as consistent with a topological organization of the flavor spectrum within MMA–DMF.

3.13 T-Neutrino: geometric seesaw anchored at $M = 100\,\text{TeV}$

Purpose. To produce neutrino mass scales compatible with oscillation data and direct bounds using the same anchored scale.

Scaling. Anchoring the geometric seesaw at the fundamental scale $M \simeq 100\,\text{TeV}$ yields a third-mass-eigenstate neutrino mass of $m_{\nu 3} \approx 0.05\,\text{eV}$, comfortably below direct kinematic limits and consistent with oscillation-scale expectations.

3.14 T-Lithium: BBN lithium-7 tension reduction

Purpose. To reduce the primordial ^{7}Li abundance prediction via a dynamical Yukawa/coupling modification within MMA–DMF without spoiling other BBN successes.

Outcome (locked). Using a dynamic Yukawa shift during BBN (parameterized by ζ in the locked configuration), the predicted primordial ^{7}Li/H is reduced to 2.8×10^{-10}, bringing the theoretical value closer to Spite-plateau observations and classifying the result as a "tension-reduced" pass.

Archived notes attribute the reduction to enhanced destruction of the ^{7}Be precursor during BBN, with the dominant pathway summarized by

$$n + {}^{7}\mathrm{Be} \;\rightarrow\; p + {}^{7}\mathrm{Li}, \tag{20}$$

followed by rapid proton burning of ^{7}Li in the same epoch. The Yukawa variation is restricted to this early-time window and leaves other light-element yields essentially unchanged.

3.15 T-Spectral-LIGO: scalar-vacuum stochastic background (locked ; null prediction)

Purpose. To estimate the gravitational-wave strain sourced by scalar-vacuum noise and verify consistency with LIGO O4 non-detection.

Step-by-step scaling derivation. Assume the scalar-vacuum contribution scales as a fraction $\beta_{\rm vac}$ of the Planck-suppressed stress-energy at the MMA–DMF anchor. Then a dimensionless strain scale at frequency f can be parametrically estimated as

$$h_{\rm rms}(f) \sim \beta_{\rm vac}\left(\frac{M}{M_{\rm Pl}}\right)^{2}\sqrt{\frac{H_0}{f}}. \tag{21}$$

Taking $\beta_{\rm vac} \sim 10^{-2}$, $M = 100\,\mathrm{TeV}$, and evaluating at $f = 100\,\mathrm{Hz}$ gives

$$h_{\rm rms}(100\,\mathrm{Hz}) \sim 10^{-37}, \tag{22}$$

far below LIGO O4 sensitivity, yielding a PASS as a null-safe consistency check.

Locked numerical check. Using the locked parameters, the resulting strain amplitude at $100\,\mathrm{Hz}$ is $h_{\rm rms} \simeq 2.5\times10^{-37}$, far below current interferometric sensitivities; the test therefore passes by predicting a null result consistent with non-detection.

3.16 T-Echo: gravitational-wave echoes from regularized cores (predictive; consolidated value reported)

Purpose. To predict echo delays from compact-object mergers if MMA–DMF regularizes the inner region and produces partial reflection.

Table 2: Consolidated constraints and test verdicts used in this work (anchored at $M =$ 100 TeV; LVK sensitivity context from [13, 16]).

Test	**Quantity**	**Computed value**	**Observational constraint**	**Margin**	**Verdict**
T-Spectral	h_{rms} (100 Hz)	2.5×10^{-37}	LVK strain sensitivity at 100 Hz $\lesssim 10^{-24}$	$> 10^{10}$ (safe)	**PASS**
T-Neutrino	m_{ν_3}	0.05 eV	KATRIN: $m_\beta < 0.8\,\mathrm{eV}$	comfortable	**PASS**
T-Lithium	^{7}Li/H	2.8×10^{-10}	Spite plateau $\approx 1.6\times10^{-10}$	tension reduced	**PASS**
Cosmology	H_0 (Early-X)	$72.1\ \mathrm{km\,s^{-1}\,Mpc^{-1}}$	SH0ES ≈ 73.0	1σ	**PASS**
Cosmology	S_8 (screening)	0.772	Weak lensing ≈ 0.77	$< 1\sigma$	**PASS**

Echo delay formula. A representative expression used is

$$\Delta t_{\mathrm{echo}} \approx 2GM \left|\ln\left(\frac{\epsilon}{2GM}\right)\right|, \qquad \epsilon \sim \frac{1}{M}. \tag{23}$$

For a $\sim 30\,M_\odot$ remnant, the consolidated MMA–DMF estimate reports

$$\Delta t_{\mathrm{echo}} \approx 32\ \mathrm{ms}. \tag{24}$$

This is presented as a distinctive, falsifiable signature relative to standard GR ringdown modeling.

Reported prediction. For a $30\,M_\odot$ remnant, the predicted echo delay is $\Delta t_{\mathrm{echo}} \approx 32\,\mathrm{ms}$ (consolidated estimate), providing a falsifiable signature distinct from standard GR ringdown.

3.17 Consolidated test table (consolidated run summary)

Table 2 reproduces the consolidated results across the primary test categories, including the missing LIGO-related and cosmology entries you explicitly flagged.

3.18 Consolidated numerical results and reproducible artifacts

Table 2 summarizes the consolidated constraints and PASS verdicts. Table 3 lists the geometric flavour spectrum used in the topological-charge clustering analysis. Table 4 reports the gravitational-wave echo delay spectrum used for the echo predictivity test. Table 5 reports the two closure tests used to formalize (i) "wave = geometric phase" and (ii) deterministic trajectories in the $\xi\to0$ limit.

Table 3: Geometric flavour spectrum used in the topological-charge clustering analysis.

Particle	Mass (GeV)	log10 Mass	Geometric charge q_f	Type	Status
Top	173.0	2.24	0.0	Quark	Anchor
Bottom	4.18	0.62	3.72	Quark	Consistent
Tau	1.78	0.25	4.58	Lepton	Consistent
Charm	1.27	0.1	4.91	Quark	Cluster_5
Muon	0.105	-0.98	7.4	Lepton	Cluster_7.5
Strange	0.093	-1.03	7.52	Quark	Cluster_7.5
Down	0.0047	-2.33	10.51	Quark	Cluster_10.5
Up	0.0022	-2.66	11.28	Quark	Cluster_11.5
Electron	0.00051	-3.29	12.73	Lepton	Cluster_13
Neutrino_3	5e-11	-10.3	28.87	Neutrino	Integer_29

Table 4: Gravitational-wave echo delay spectrum for a regularized-core scenario. The detectability column is an *illustrative* qualitative classification based on order-of-magnitude sensitivity considerations (not a full matched-filter pipeline).

Mass ($M_\odot$)	**Echo delay (ms)**	**Amplitude ratio**	**Indicative detectability**
5.0	5.3	0.12	Potentially detectable (next-gen)
10.0	10.7	0.18	Potentially detectable (next-gen)
30.0	32.1	0.35	Potentially detectable (future run)
50.0	53.5	0.42	Potentially detectable (future run)
65.0	69.2	0.45	High SNR (forecast)

4 Discussion

4.1 Positioning, audit language, and scope

Several accompanying notes use "audit" and "verdict" language (e.g., *PASS*, *locked*, *mature*) to summarize internal consistency checks across the full test battery. In this manuscript we treat these statements as *engineering-style summaries* of the reproducible artifacts packaged with the submission, not as a substitute for independent replication. Where the notes express strong qualitative judgments (e.g., "paradigm shift" or "smoking-gun"), we restate them as concrete, falsifiable predictions. Examples include (i) mass-dependent gravitational-wave echo delays for regularized cores, (ii) a high-frequency roll-off of Bell-type correlations under rapid context switching set by the vacuum relaxation time, and (iii) the operational disappearance of interference when the local functional coupling $\omega_c(\phi)$ is replaced by a constant control.

The broader motivation reflected in the notes is a critical stance toward models that introduce multiple unconstrained "dark" components to reconcile tensions. Regardless of that motivation, the scope of this work is narrower and technical: to document a single fixed-scale ($M = 100$ TeV) 0–DOF configuration, the equations used in the numerical experiments, and a reproducible battery of tests spanning microphysics, astrophysical signatures, and cosmological anchors. Independent replication and likelihood-level confronta-

Table 5: Metrics for the closure tests: phase-equivalence (wave = geometric phase) and determinism in the $\xi \to 0$ limit.

Test ID	Metric	Value
WPD-TEST1-PHASE-EQUIVALENCE	metric_on_rms_domega_dt	1.0315607877947948
WPD-TEST1-PHASE-EQUIVALENCE	metric_off_rms_domega_dt	7.862267668068157e-09
WPD-TEST1-PHASE-EQUIVALENCE	ratio_on_over_off	131203977.1915143
WPD-TEST1-PHASE-EQUIVALENCE	verdict	PASS
QT-TEST2-XI-TO-ZERO	determinism_rms_diff_xi0	0.0
QT-TEST2-XI-TO-ZERO	determinism_max_diff_xi0	0.0
QT-TEST2-XI-TO-ZERO	ensemble_var_final_x	2.738967108038788e-06
QT-TEST2-XI-TO-ZERO	ensemble_std_final_x	0.0016549825098890888
QT-TEST2-XI-TO-ZERO	verdict	PASS
OVERALL	overall_verdict	PASS

tions with raw datasets are explicitly left as next steps.

5 Conclusions

Key interpretational takeaways. Across the fixed suite of internal-consistency checks and numerical validations, the project-level conclusion can be summarized as follows:

1. **The "wave" is an effective geometric-phase phenomenon**: it is the manifestation of non-Markovian scalar-vacuum memory and path-dependent phase accumulation. When the geometric coupling is disabled, wave-like behavior disappears.

2. **The "particle" is the ontic carrier**: it is stabilized as a localized (topological) energy-density excitation, governed by an environment-dependent effective mass.

3. **Quantum randomness is treated as epistemic**: stochasticity is relegated to incomplete knowledge of vacuum-noise initial conditions, preserving fundamental determinism in the $\xi \to 0$ limit.

Within the MMA–DMF framework anchored at $M = 100\,\text{TeV}$, wave–particle duality and quantum-trajectory phenomenology emerge as effective statistics of a deterministic scalar dynamics closed by a fluctuation–dissipation kernel. Across the documented test suite, MMA–DMF passes internal reproducibility checks and avoids immediate observational contradictions. The framework yields concrete, falsifiable predictions in contextuality roll-off under ultra-fast switching and gravitational-wave echo delays, while remaining null-safe for present LIGO O4 stochastic-background sensitivity. Future work should prioritize direct data-likelihood implementations, controlled systematics, and experimental designs that can isolate MMA–DMF-specific signatures.

Data and Code Availability

All code, configurations, datasets, and build artifacts required to reproduce the figures, tables, and pass/fail metrics reported in this manuscript are publicly archived on Zenodo (DOI: 10.5281/zenodo.17993144). The archive includes (i) this LaTeX source, (ii) analysis/diagnostic scripts, (iii) CSV/JSON outputs used to build tables, and (iv) a SHA-256 manifest (Appendix D) to verify bit-exact integrity. The fixed parameter set used throughout is reported in Table 1. All results in this manuscript correspond to executed runs under that fixed configuration (no provisional entries).

Reproduction entry points. Representative commands (from the project root) are:

- `python code/mma_dmf_validation.py` (microphysical determinism and phase/coupling checks; exports the verdict JSON and metrics CSV in `data/`).
- `python code/Hello_World_Test_Protocols_WPD1_and_QT1.py` and `python code/Hello_World` (WPD/QT trajectory protocols and statistics).
- `python code/test_t_echo_delay_spectrum_with_notes.py` (regenerates Table 4 from `data/test_t_echo_delay_spectrum.csv`).
- `python code/test_t_magis_decoherence.py` and `python code/test_t_context_dynamic.py` (macrorealism-gate and contextuality roll-off checks).

Integrity. Appendix D lists SHA-256 checksums for the principal scripts and data files used to generate this manuscript.

A Appendix A: Effective envelope reduction (outline)

Write the scalar as a slowly varying complex envelope times a fast carrier:

$$\phi(x,t) = \Re\Big[\psi(x,t)\, e^{-i\Theta(x,t)}\Big], \tag{25}$$

with Θ from Equation (7). Insert (25) into the linearized sector of (1), expand assuming $|\partial_t\psi| \ll \omega_c|\psi|$, and average over the carrier period. The leading-order balance cancels the fast oscillation, and the next-order terms yield an effective Schrödinger-type envelope equation with $\hbar_{\mathrm{eff}}$ and m_{eff} fixed by the same closure that defines D in (4). This is the operational basis for WPD and QT tests: wave dynamics is an emergent envelope approximation whose phase structure is geometric.

B Appendix B: LIGO O4 null prediction derivation (expanded)

Starting from the assumption that the scalar vacuum sources metric perturbations suppressed by M_{Pl}, a stress-energy fluctuation δT produces $h \sim \delta T / M_{\text{Pl}}^2$ (up to geometric factors). Taking δT to scale as $\beta_{\text{vac}} M^4$ over coherence time $\sim 1/f$ and folding in cosmological dilution via $\sqrt{H_0/f}$ yields Equation (21). Evaluated at $f = 100\,\text{Hz}$, the resulting strain is Equation (22), far below LIGO O4.

C Appendix C: Echo delay expression

Equation (23) follows the standard logarithmic time-delay scaling for near-horizon reflection in compact-object echo phenomenology when a reflective surface sits at $r = 2GM + \epsilon$ with $\epsilon \ll 2GM$. In MMA–DMF, $\epsilon \sim 1/M$ provides a natural microscopic regulator tied to the same anchor scale.

D Reproducibility artifacts

Table 6: Reproducibility artifacts packaged with this manuscript and their SHA-256 checksums.

Artifact (path in archive)	**SHA-256**
`code/Hello_World_Test_Protocols_WPD1_and_QT1.py`	`f464d3e6d5d5489fec2441f4ba7b0d09698` `72e585f3684853dc518337a4bbbca`
`code/Hello_World_Test_QT1_Quantum_Trajectory_` `Statistics.py`	`50a198e34dab88858341b8c9fd69ca839ec` `f1e7cfcf8eaae6cd5d9c9ea938151`
`code/mma_dmf_double_slit_solver.py`	`fa2284c9b9041cf16895007f4ba2341f9d4` `26a9104c89d58062a68abeae9cf82`
`code/mma_dmf_validation.py`	`7b2c3a15f43539f0f0a59776eddbdd84580` `be5b53b438a2dd5f66d301bfa063c`
`code/mma_dmf_microphysics_core.py`	`92a439f4355e585720d59d1cc6a68f79ba9` `5be2ed6203a541fc8b46d8b12511b`
`code/test_t_context_dynamic.py`	`c8da394a9638fe09d480adc95f2ecea0944` `019bada322696d4460a555b54b96d`
`code/test_t_magis_decoherence.py`	`52255d75c6fd6a219bcb715c305879fd6c2` `87695fe95acfb7ea506c2de8ddd3a`
`code/test_t_echo_delay_spectrum_with_notes.py`	`8402e12edc6be1ad16faadbcb17f900871b` `f79e1a8d2db9114989eec41c73429`
`data/mma_dmf_wpd_qt_final_test_metrics.csv`	`c448d529ccfc7461edcbe7e6546bd96e04b` `511ac1060ad1067c8b7a4eb68a13b`
`data/mma_dmf_wpd_qt_final_test_verdicts.json`	`6aae2bd043afdb204725e08d87134cb6d11` `bfa542c0d113d61768be8a903c41b`
`data/mma_dmf_consolidated_results_table.csv`	`3a68f2bb50d02e4a2d7ff30e32b7e10def2` `d27bcd590c891539630521d682a44`

A Implementation and audit notes (engineering constraints)

This appendix consolidates implementation-critical constraints and "engineering" motivations recorded in the project audit logs (consolidated archive). These notes do not introduce additional degrees of freedom; they clarify numerical stability, physical consistency constraints, and the pass/fail metrics used to validate the tests reported in the main text.

A.1 Microphysics bridge: phase-lock approximation

For cosmological scaling checks a coarse-grained "fluid" approximation for the scalar sector is sufficient, but the microphysical trajectory tests require a *phase-lock* approximation: ϕ is treated as the carrier of *local phase information* that drives the guidance dynamics. Operationally, wave-like observables are recovered through integrated phase accumulation along trajectories and disappear when the coupling that generates the phase functional is disabled (Test 1 in the main text).

A.2 Relativistic guidance constraint (subluminality near nodes)

Near wavefunction nodes (or, equivalently, regions with steep density gradients), naive guidance laws can generate unphysical superluminal velocities. The audit notes recommend enforcing subluminality by including an explicit Lorentz factor in the guidance term,

$$v_i \;\to\; \frac{\nabla_i S}{m\,\gamma} - \frac{D_{ij}}{\rho\,\gamma}\,\nabla_j \rho, \qquad \gamma \equiv \frac{1}{\sqrt{1-v^2}}, \tag{26}$$

which suppresses velocity growth in large-$\nabla\rho$ regions without altering the deterministic $\xi \to 0$ limit.

A.3 Numerical stability: the "ringing" (Gibbs) ghost and smooth guards

The audit logs document that discontinuous switches (hard `if/else` thresholds or Heaviside-type steps) triggered spectral Gibbs ringing in time evolution and in higher-order derivatives. The practical requirement is therefore to use C^∞ activation functions for regime transitions, such as the smooth guard used in this work,

$$\mathcal{S}_{\rm guard}(\rho) = \tanh\left[\left(\frac{\rho}{\rho_{\rm crit}}\right)^2\right], \tag{27}$$

to avoid numerical artifacts that can masquerade as physical oscillations.

A.4 Explicit success metrics recorded in the audits

The audits specify quantitative pass criteria used to label tests as PASS:

- **Born recovery (QT-1):** the Kullback–Leibler divergence between the final trajectory histogram and the Born target density must satisfy $D_{\mathrm{KL}} < 0.05$ for the locked configuration reported here.
- **Thermal closure (FDT stability test):** long-run energy drift must satisfy $|\text{slope}| < 10^{-5}$ to exclude spurious scalar "heating" or "freezing".

A.5 Astrophysical anchoring notes used for the spectral drift check

For the magnetar/FRB spectral drift check ("sad trombone"), the audit notes tie the characteristic drift scale $\mathrm{d}\nu/\mathrm{d}t \sim -200$ MHz/ms to an order-of-magnitude magnetar flare energy release $\sim 10^{40}$ erg and the corresponding scalar relaxation timescale. In the manuscript this is treated as an internal, order-of-magnitude calibration consistent with the reported phenomenology.

A.6 Contextuality as finite vacuum-memory delay

The dynamic contextuality roll-off is interpreted as a consequence of finite vacuum memory: the effective correlation time τ_{vac} sets the scale at which rapid measurement-context switching suppresses nonclassical correlations. Operationally, for switching frequencies above $1/\tau_{\mathrm{vac}}$ the CHSH parameter approaches the classical bound $S \to 2.0$, consistent with the roll-off test reported in the main text.

A.7 Echoes as a distinctive falsifiable signature

The audit narrative highlights gravitational-wave echoes as a high-leverage discriminator: a nonzero post-merger echo train (e.g., the ~ 32 ms delay quoted for a $30\,M_{\odot}$ target) would provide a distinctive signature relative to classical "silent" ringdown expectations. In this work we present the echo delay spectrum as a falsifiable prediction and report the associated internal amplitude proxy as an order-of-magnitude quantity.

A.8 Golden-set detail values used in the consolidated runs

For convenience, the audit logs emphasize two microphysical values used throughout the locked runs: the geometric neutrino charge $q_{\nu 3} = 28.8$ (yielding $m_{\nu 3} \simeq 0.05$ eV) and the BBN Yukawa shift $\zeta_{\mathrm{BBN}} = -0.01$ used to reduce the primordial ^{7}Li tension while leaving other light-element yields approximately unchanged.

AI and Automation Disclosure

AI-assisted tools were used to accelerate production tasks (figure drafts, plotting/analysis scripts, and code scaffolding). All scientific claims, numerical results, and final figures/tables were verified and curated by the author.

Conflicts of Interest

The author declares no conflicts of interest.

References

[1] M. Born, "Zur Quantenmechanik der Stoßvorgänge", *Zeitschrift für Physik* **37** (1926) 863–867.

[2] D. Bohm, "A Suggested Interpretation of the Quantum Theory in Terms of 'Hidden' Variables I–II", *Physical Review* **85** (1952) 166–193.

[3] E. Nelson, "Derivation of the Schrödinger Equation from Newtonian Mechanics", *Physical Review* **150** (1966) 1079–1085.

[4] J. S. Bell, "On the Einstein Podolsky Rosen Paradox", *Physics Physique Fizika* **1** (1964) 195–200.

[5] J. F. Clauser, M. A. Horne, A. Shimony, and R. A. Holt, "Proposed Experiment to Test Local Hidden-Variable Theories", *Physical Review Letters* **23** (1969) 880–884.

[6] S. Kocsis *et al.*, "Observing the Average Trajectories of Single Photons in a Two-Slit Interferometer", *Science* **332** (2011) 1170–1173.

[7] J. W. T. Hessels *et al.*, "FRB 121102 Bursts Show Complex Time–Frequency Structure", *The Astrophysical Journal Letters* **876** (2019) L23.

[8] Planck Collaboration, "Planck 2018 Results. VI. Cosmological Parameters", *Astronomy & Astrophysics* **641** (2020) A6.

[9] A. G. Riess *et al.*, "A Comprehensive Measurement of the Local Value of the Hubble Constant with 1 km s^{-1} Mpc^{-1} Uncertainty from the SH0ES Team", *Astrophysical Journal Letters* **934** (2022) L7.

[10] B. D. Fields, K. A. Olive, T.-H. Yeh, and C. Young, "Big-Bang Nucleosynthesis after Planck", *Journal of Cosmology and Astroparticle Physics* **03** (2020) 010.

[11] KATRIN Collaboration, "Improved Upper Limit on the Neutrino Mass from a Direct Kinematic Method by KATRIN", *Physical Review Letters* **123** (2019) 221802.

[12] MAGIS Collaboration. *MAGIS-100: A Matter-Wave Atomic Gradiometer Interferometric Sensor for Precision Inertial Measurements*. Quantum Science and Technology **6**, 044003 (2021). arXiv:2104.02835. DOI: 10.1088/2058-9565/abf719.

[13] B. P. Abbott *et al.* (LIGO Scientific Collaboration and Virgo Collaboration), "Prospects for Observing and Localizing Gravitational-Wave Transients with Advanced LIGO, Advanced Virgo and KAGRA", *Living Reviews in Relativity* **23** (2020) 3.

[14] R. Abbott *et al.* (LIGO Scientific Collaboration and Virgo Collaboration), "Upper Limits on the Isotropic Gravitational-Wave Background from Advanced LIGO's and Advanced Virgo's Third Observing Run", *Physical Review D* **104** (2021) 022004.

[15] V. Cardoso and P. Pani, "Testing the Nature of Dark Compact Objects: A Status Report", *Living Reviews in Relativity* **22** (2019) 4.

[16] R. Abbott et al. (LIGO Scientific Collaboration, Virgo Collaboration, and KAGRA Collaboration). *Upper limits on the isotropic gravitational-wave background from Advanced LIGO's and Advanced Virgo's fourth observing run (O4a).* arXiv:2508.20721 (2025).